nanomaterials

MDPI

Article

Enhanced Electrochemical Properties and OER Performances by Cu Substitution in $NiCo_2O_4$ Spinel Structure

Hyerim Park [1], Byung Hyun Park [1], Jaeyoung Choi [1], Seyeon Kim [1], Taesung Kim [1], Young-Sang Youn [1], Namgyu Son [1,*], Jae Hong Kim [2] and Misook Kang [1,*]

[1] Department of Chemistry, College of Natural Sciences, Yeungnam University, Gyeongsan 38541, Gyeongbuk, Korea; ilkilhs1329@ynu.ac.kr (H.P.); pbh0326@ynu.ac.kr (B.H.P.); hty555@naver.com (J.C.); ksy4219@naver.com (S.K.); ktsart@naver.com (T.K.); ysyoun@yu.ac.kr (Y.-S.Y.)

[2] School of Chemical Engineering, College of Engineering, Yeungnam University, Gyeongsan 38541, Gyeongbuk, Korea; jaehkim@ynu.ac.kr

* Correspondence: sng1107@ynu.ac.kr (N.S.); mskang@ynu.ac.kr (M.K.); Tel.: +82-053-810-3798 (N.S.); +82-053-810-2363 (M.K.)

Received: 11 August 2020; Accepted: 28 August 2020; Published: 31 August 2020

Abstract: In order to improve the electrochemical performance of the $NiCo_2O_4$ material, Ni ions were partially substituted with Cu^{2+} ions having excellent reducing ability. All of the electrodes were fabricated by growing the $Ni_{1-x}Cu_xCo_2O_4$ electrode spinel-structural active materials onto the graphite felt (GF). Five types of electrodes, $NiCo_2O_4$/GF, $Ni_{0.875}Cu_{0.125}Co_2O_4$/GF, $Ni_{0.75}Cu_{0.25}Co_2O_4$/GF, $Ni_{0.625}Cu_{0.375}Co_2O_4$/GF, and $Ni_{0.5}Cu_{0.5}Co_2O_4$/GF, were prepared for application to the oxygen evolution reaction (OER). As Cu^{2+} ions were substituted, the electrochemical performances of the $NiCo_2O_4$-based structures were improved, and eventually the OER activities were also greatly increased. In particular, the $Ni_{0.75}Cu_{0.25}Co_2O_4$/GF electrode exhibited the best OER activity in a 1.0 M KOH alkaline electrolyte: the cell voltage required to reach a current density of 10 mA cm^{-2} was only 1.74 V (η = 509 mV), and a low Tafel slope of 119 mV dec^{-1} was obtained. X-ray photoelectron spectroscopy (XPS) analysis of $Ni_{1-x}Cu_xCo_2O_4$/GF before and after OER revealed that oxygen vacancies are formed around active metals by the insertion of Cu ions, which act as OH-adsorption sites, resulting in high OER activity. Additionally, the stability of the $Ni_{0.75}Cu_{0.25}Co_2O_4$/GF electrode was demonstrated through 1000th repeated OER acceleration stability tests with a high faradaic efficiency of 94.3%.

Keywords: oxygen evolution reaction; Cu substitution; spinel structure; oxygen vacancy

1. Introduction

With the increase in environmental pollution due to excessive use of fossil fuels, studies on new energy conversion and storage systems such as water decomposition devices, fuel cells, and batteries are actively being conducted. In particular, hydrogen energy produced by water splitting is an ideal clean energy and has the advantage of having the largest energy efficiency per unit mass compared to other energy sources [1]. In general, electrolysis of water includes a hydrogen evolution reaction (HER) and an oxygen evolution reaction (OER). In particular, the OER process requires high over-potential, which negatively affects the overall reaction process [2]. It is known that noble metal materials can reduce the over-potential, and in fact, noble metals such as Ir and Ru are already used as efficient electrode active materials [3,4]. However, these noble metals are limited to commercialization on a large scale due to their high price and low reserves, so it is urgent to develop an OER electrode active material with low cost, high efficiency, and high stability for efficient hydrogen production. Recently,

Co-based bimetal oxides having a spinel structure as a non-noble metal active material have attracted wide attention in the field of energy storage and conversion.

As an electrode active material for OER, many transition metal compounds having various ligands such as oxide, hydroxide, and phosphide are used [5–7], of which Co-based metal oxide is the most promising OER electrode active material available in alkaline media. Moreover, doping a metal ion such as Ni or Fe with a Co-based oxide can further improve electrocatalytic performance. Among them, $NiCo_2O_4$ has high electrical conductivity and stability, attracting much attention from scientists, and is known as a reliable OER electrode active material with excellent repeatability [8]. The general structural formula of a unique spinel structure such as $NiCo_2O_4$ is ACo_2O_4, where A is a divalent metal ion such as Ni, Fe, Mn, Mg and Zn, and a cubic packing structure connected to O, where Co^{3+} and A^{2+} ions are respectively the centers of octahedral and tetrahedral [9]. Nickel-cobalt bimetal oxide ($NiCo_2O_4$) is a material that has been studied extensively for a long time and shows ideal electrochemical performance in super capacitors or batteries such as LiB [10], Zn-Air [11], and Li-Air [12]. Recently, $NiCo_2O_4$ has been quite favored in OER, HER, ORR(Oxygen Reduction Reaction), and alcohol oxidation reactions by several researchers [13–16]. It has been found so far that the electrode potential required to drive a current density of 10 mA cm^{-2} in a $NiCo_2O_4$ electrode active material loaded on a Ni foam support is about 360 mV [17]. Although many researchers are changing the synthetic method and the support to change the high conductivity and active surface area, it has been found that the intrinsic activity of the $NiCo_2O_4$ electrode active material has not improved significantly.

In this study, in order to improve the electrochemical performance of the $NiCo_2O_4$ electrode active material, Ni ions were partially substituted with Cu ions having excellent reducing ability. In 1999, Tavares and his colleagues concluded that the substitution of Cu(II) in the $NiCo_2O_4$ spinel lattice leads to significant changes in surface composition and oxygen evolution [18]. Meanwhile, Mugheri et al. also reported OER performance on $NiCo_2O_4$/CuO electrode active material: 0.5 g of CuO on $NiCo_2O_4$ showed a low starting potential of 1.46 V, and a current density of 10 mA cm^{-2} was achieved at an electrode potential of 230 mV, and the durability was maintained for 35 h [19]. On the other hand, due to the similar physical properties of Ni and Co, the preparation of nickel-cobalt bimetal oxide of $NiCo_2O_4$ is relatively simple and a pure phase structure is easily formed. Synthesis methods vary from sol–gel, chemical precipitation, spray pyrolysis, and electrospinning methods, but many researchers have been the solvothermal or hydrothermal synthesis methods, which are a relatively efficient method to produce $NiCo_2O_4$ nanomaterials [20,21]. In addition, nanoparticles of $NiCo_2O_4$ have various morphologies such as nanowires, nanorods, nanosheets, nanoparticles, hollow nanospheres, and 3-D nanoflowers, and the electrochemical properties vary depending on the morphologies [22,23]. In our study, the graphite felt (GF) electrode support was hydrothermally treated with metal precursors of electrode active materials in synthetic solution. An electrode made by stably growing $NiCo_2O_4$ or $Ni_{1-x}Cu_xCo_2O_4$ nanoparticles on a GF support was used as a water electrolysis catalyst. Moreover, instead of Ni in the $NiCo_2O_4$ spinel structure, Cu was partially substituted, the optimal amount was confirmed, and the OER performance was checked to investigate their correlation.

2. Materials and Methods

2.1. Fabrications of $NiCo_2O_4$/GF and $Ni_{1-x}Cu_xCo_2O_4$/GF Electrodes

OER electrodes are manufactured by growing active material nanoparticles on the surface of the support electrode by the hydrothermal method as shown in Scheme 1A GF030 (Graphite Felt (GF), 3 mm, CeTech Co., Wuri Dist., Taichung City, Taiwan) was used as an electrode support, and was cut to a width × length × thickness of 10 mm × 10 mm × 1.5 mm. As shown in Scheme 1B, the GF was thermally stabilized by heating at 800 °C at a rate of 5 °C min^{-1} using a thermogravimetric analyzer (TGA, TGA-N1000, Sinco, Daejeon, Korea) under air atmosphere. As a result, it was confirmed that there was almost no decrease in mass to a temperature of 500 °C [24]. Before the nanoparticles

were coated, in order to remove the oil film or organic impurities on the surface of the electrode support, it was heated up to 450 °C at a rate of 10 °C min^{-1} in an electric furnace and held at 450 °C for 3 h. After cooling, the surface was etched by ultrasonic treatment for 30 min in a strong acid solution to facilitate coating of the electrode active material. After washing with deionized water and ethanol several times, it was dried in a vacuum oven at 110 °C for 6 h.

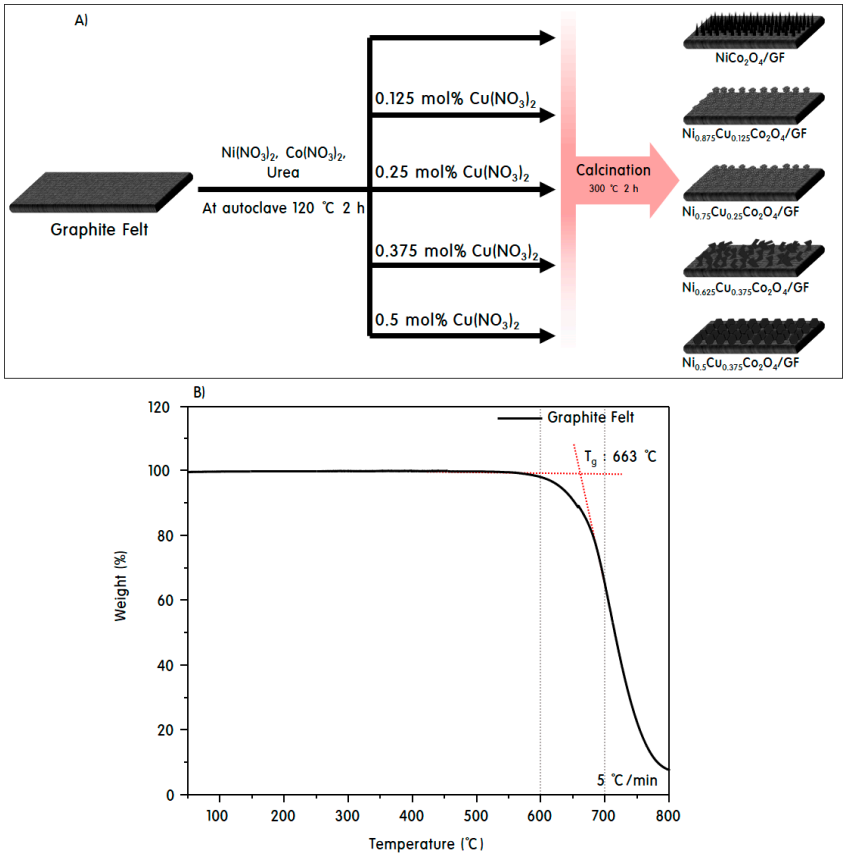

Scheme 1. (**A**) Synthesis of $Ni_{1-x}Cu_xCo_2O_4$/graphite felt (GF). (**B**) Graphite felt air atmosphere TGA analysis.

First, the hydrothermally fabrication method of the $NiCo_2O_4$/GF electrode is as follows: 10 mmol of $Ni(NO_3)_2{\cdot}6H_2O$ (≥98%, Junsei, Tokyo, Japan) and 20 mmol of $Co(NO_3)_2{\cdot}6H_2O$ (≥98%, Junsei, Tokyo, Japan) were dissolved in 50 mL distilled water for 1 h. Into the uniformly mixed solution, 0.2 mol of urea (≥98%, Junsei, Tokyo, Japan) was added and stirred for 2 h at room temperature. The GF support electrode was put into this solution, and was sonicated for 6 h to allow the solution to sufficiently penetrate into the support electrode. The final solution is transferred to an autoclave, and the temperature is raised to 120 °C at a heating rate of 5 °C min^{-1} and maintained for 3 h. After the reaction is completed, it is cooled to room temperature and opened to confirm that the electrode active material is coated on the support electrode. It was confirmed that the surface of the obtained electrode was coated with a light purple color, which was washed several times with water and ethanol and then dried at 70 °C for 12 h. Finally, the $NiCo_2O_4$/GF electrode fabrication is completed through the calcination step at 350 °C for 3 h in an air atmosphere.

In the next step, $Ni_{1-x}Cu_xCo_2O_4$/GF (x = 0.125, 0.25, 0.375, and 0.5) electrodes were also made in the same way as $NiCo_2O_4$/GF electrode fabrication. Of $Ni(NO_3)_2{\cdot}6H_2O$ 8.75, 7.50, 6.25, and 5.00 mmol, 1.25, 2.50, 6.25, and 5.00 mmol of $Cu(NO_3)_2{\cdot}6H_2O$ (≥98%, Junsei, Tokyo, Japan), and 0.02 mol of $Co(NO_3)_2{\cdot}6H_2O$ were dissolved in 50 mL of distilled water and stirred for 1 h. Of urea 0.2 mol was added to the uniformly mixed solutions and stirred for 2 h at room temperature. Here, the GF support electrodes were put in the solutions, and those were ultrasonic treated for 6 h. The final solutions

containing GF support electrodes were transferred to autoclaves, heated to 120 °C at a rate of 5 °C min^{-1} and maintained for 3 h. After completion of the reaction, the mixtures were cooled to room temperature, and it was confirmed that the electrode active materials were well loaded on the support electrodes. It was convinced that the electrode active materials were coated on the support electrode surfaces, since the electrode surfaces turned from light purple to light brown. In particular, the brown colors of the electrode surfaces were noticeable according to the content of Cu. The electrodes were washed several times with water and ethanol, and then dried at 70 °C for 12 h. Finally, a $Ni_{1-x}Cu_xCo_2O_4$/GF electrodes were obtained through calcination processes at 350 °C for 3 h in air atmospheres. The amount of active materials loaded on the GF support electrode was 10 mg, which was constant for all electrodes.

2.2. Evaluation of Physicochemical Properties of Electrodes

Crystal structures of the $Ni_{1-x}Cu_xCo_2O_4$ active material grown on the GF support electrode were confirmed by XRD (Miniflex, Rigaku, Tokyo, Japan) using nickel-filtered Cu *Kα* radiation (30 kV, 15 mA) in the 2θ range of 20–90°. The surface morphologies of these active materials were observed with a Hitachi S-4100 field emission scanning electron microscope (SEM). Energy dispersive X-ray spectroscopy (EDS) and EDS elemental mapping were performed by EDAX (EX-250, Horiba, Tokyo, Japan) to know the composition of the elements constituting the $Ni_{1-x}Cu_xCo_2O_4$ active materials. The determinant analysis and SAED pattern for the best performing active material were investigated with a high-resolution transmission electron microscopy (HR-TEM, FEI's Titan G2 STEM, FEI Company, Hillsboro, Oregon, USA) instrument. The oxidation states of the elements present in the electrode active materials before and after the OER reaction were confirmed using X-ray photoelectron spectroscopy (XPS, K-Alpha Compact XPS, Al *Kα* 1486.6 eV, Thermo Scientific, Waltham, MA, USA).

2.3. Electrochemical Characterizations of Electrodes

All electrochemical measurements were performed with an electrochemical cell test system (IVIUMnSTAT, Ivium technologies, Eindhoven, Netherlands) at room temperature of 25 °C. The electrochemical OER activity was performed using a standard 3-electrode type electrochemical device, and was performed in an alkaline electrolyte (1.0 M KOH, pH = 14). Here, $Ni_{1-x}Cu_xCo_2O_4$/GF as a working electrode, Hg/Hg_2Cl_2 (saturated caramel electrode, SCE) as a reference electrode, and a Pt wire having a thickness of 0.2 mm as a counter electrode were used, respectively. Linear sweep voltammetry (LSV) measurements were performed at a scan rate of 5 mV s^{-1} at 1.0 M KOH (pH = 14). Electrochemical impedance spectroscopy (EIS) measurements were made by applying an amplitude range of 5 mV at frequencies ranging from 100 kHz to 0.01 Hz. Electrochemically active surface area (ECSA) measurements were performed at varying scan speeds from 10 to 100 mV s^{-1} in the 0.967–1.067 V_{RHE} range. The long-term stability test was confirmed by measuring the change in voltage by applying a current of 10 mA cm^{-2}. To calculate the Faradaic efficiency, a closed reactor was constructed and used for the OER reaction, and the gases inside the reactor were sampled for 4 h at 30 min intervals using a microsyringe. The sampled gases were injected into gas chromatography (GC, Master GC, Scinco, Daejeon, Korea) equipped with a thermal conductivity detector (TCD), and the amount of oxygen gas generated after the OER reaction was analyzed. The measured potential was converted to reversible hydrogen electrode potential (VRHE) using the following calibration equation [25].

$$V_{RHE} = V_{SCE} + 0.241 + 0.059 \times pH \quad (1)$$

3. Results and Discussion

3.1. Physicochemical Properties of $Ni_{1-x}Cu_xCo_2O_4$ Electrode Active Materials Grown on GF

XRD patterns of $Ni_{1-x}Cu_xCo_2O_4$ electrode active materials grown on the support electrode surface are compared in Figure 1. $NiCo_2O_4$ was consistent with the cubic spinel structure (JCPDS card no. 01-073-1702) with a space group of Fd-3m, peaks corresponding to (111), (220), (311), and (400) facets

were observed at 2-theta = 18.9°, 31.2°, 36.7°, and 44.6° [26]. $NiCo_2O_4$ is a p-type semiconductor having a band gap of 2.1 eV, and is a ferrimagnetic material having a number of oxidation–reduction states and excellent electrical conductivity. Ni cations occupy octahedral sites, whereas Co cations coexist in tetrahedral and octahedral sites, so they can be expressed in the form of $[Co^{2+}][Ni^{3+}Co^{3+}]O_4$ [27]. In a conventional unit cell of the AB_2O_4 spinel structure, O atoms are arranged in a face centered cubic lattice, and there are tetrahedral (8A) sites and octahedral (16B) sites available for the cations. If metal atoms occupy the 8A sites and Co atoms occupy the 16B sites, then the structure is named normal spinel. Conversely, if M atoms occupy half of the 16B sites, while Co atoms occupy the 8A sites and the left half of the 16B sites, then the structure is named inverse spinel. Therefore, it can be said that $NiCo_2O_4$ has a typical inverse spinel structure [28]. Here, if a part of the Ni metal is replaced with Cu^{2+} ions, the Cu^{2+} ions do not occupy the Ni^{2+} sites, but are substituted at the tetrahedral sites of Co^{2+}, and the Co ions occupying the tetrahedral sites move to the octahedral sites of the empty Ni^{3+} [29]. In conclusion, $Ni_{1-x}Cu_xCo_2O_4$ crystals in which Ni is partially substituted with Cu can be accurately expressed as $(Co^{2+}{}_{1-x}Cu^{2+}{}_x)^{tet}(Ni^{3+}{}_{1-x}Co^{3+}{}_{1+x})^{oct}O_4$. All of $Ni_{1-x}Cu_xCo_2O_4$ materials substituted with Cu^{2+} in the XRD pattern also showed cubic spinel crystals with a space group of Fd-3m. However, these coincide with the peaks at 2-theta = 19.1°, 31.4°, 37.0°, and 45.1° corresponding to (111), (220), (311), and (400) facets of $CuCo_2O_4$ (JCPDS No. 00-001-1155), which are shifted at a higher angle compared to the peaks of the $NiCo_2O_4$ crystals [30]. This is due to the different bond distances and angles between Metal-O due to the different radius of Cu, Co, and Ni ions. According to Bragg's equation, the shift of the peak at a high angle by substitution of Cu means that it has a smaller d-spacing [31]. Meanwhile, it is well known, the degree of spinel inversion, defined as the proportion of Ni ions on the Oh site, was found to be critical for high conductivity [32]. Therefore, how much the Ni^{3+} occupied at the octahedral site changes due to Cu substitution will be a factor in measuring conductivity.

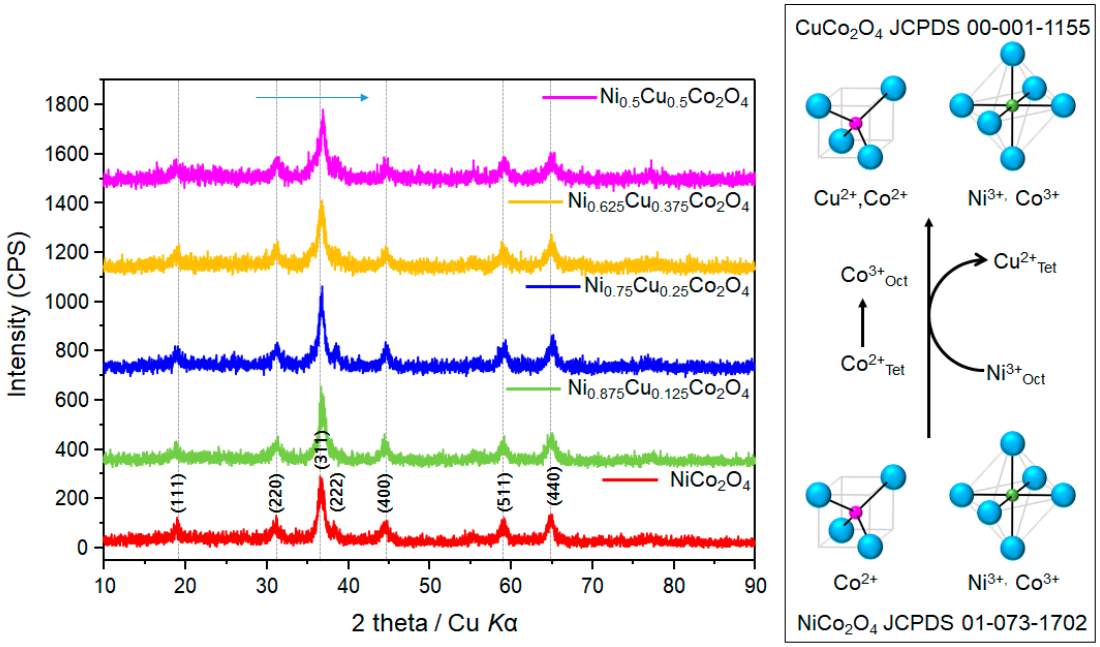

Figure 1. XRD pattern of synthesized $Ni_{1-x}Cu_xCo_2O_4$ active materials.

Figure 2 shows the morphologies of the GF surface and $Ni_{1-x}Cu_xCo_2O_4$ electrode active materials grown on the GF surface. The surface of the pure GF support electrode was smooth overall, and scratches were partially visible on the surface. From this, it was confirmed that the support electrode surface was well etched through heat and acid treatment in the precoating treatment step. On the surface of the $NiCo_2O_4$/GF electrode, small nanorods corresponding to 500 nm in length grew sprawling like

dense hairs. However, as Cu was substituted for Ni, the nanorod shaped particles disappeared and the particles with angular plate appeared. The rod and plate shape were mixed until the substitution amount of Cu was 0.375 mol, and the crystal growth was not high compared to $NiCo_2O_4$. It seems that irregular crystals with various sizes and various particle shapes were grown on the GF surface by partially inhibiting the growth between Ni-O-Co as Cu was substituted at the Ni site during the crystal growth process. As a result, it is believed that the irregularity of the crystal shape can lower the activation energy of the reaction by increasing the surface area and the number of reaction active sites [33]. However, in the $Ni_{0.5}Cu_{0.5}Co_2O_4$/GF electrode where Cu and Ni were added 1:1, regular $Ni_{0.5}Cu_{0.5}Co_2O_4$ particles with a square plate with a thickness of 70–150 nm and a width of 700 nm were grown on the GF support electrode. It has been confirmed that these largely grown particles are expected to be a factor to lower the electrode performance by increasing the surface resistance.

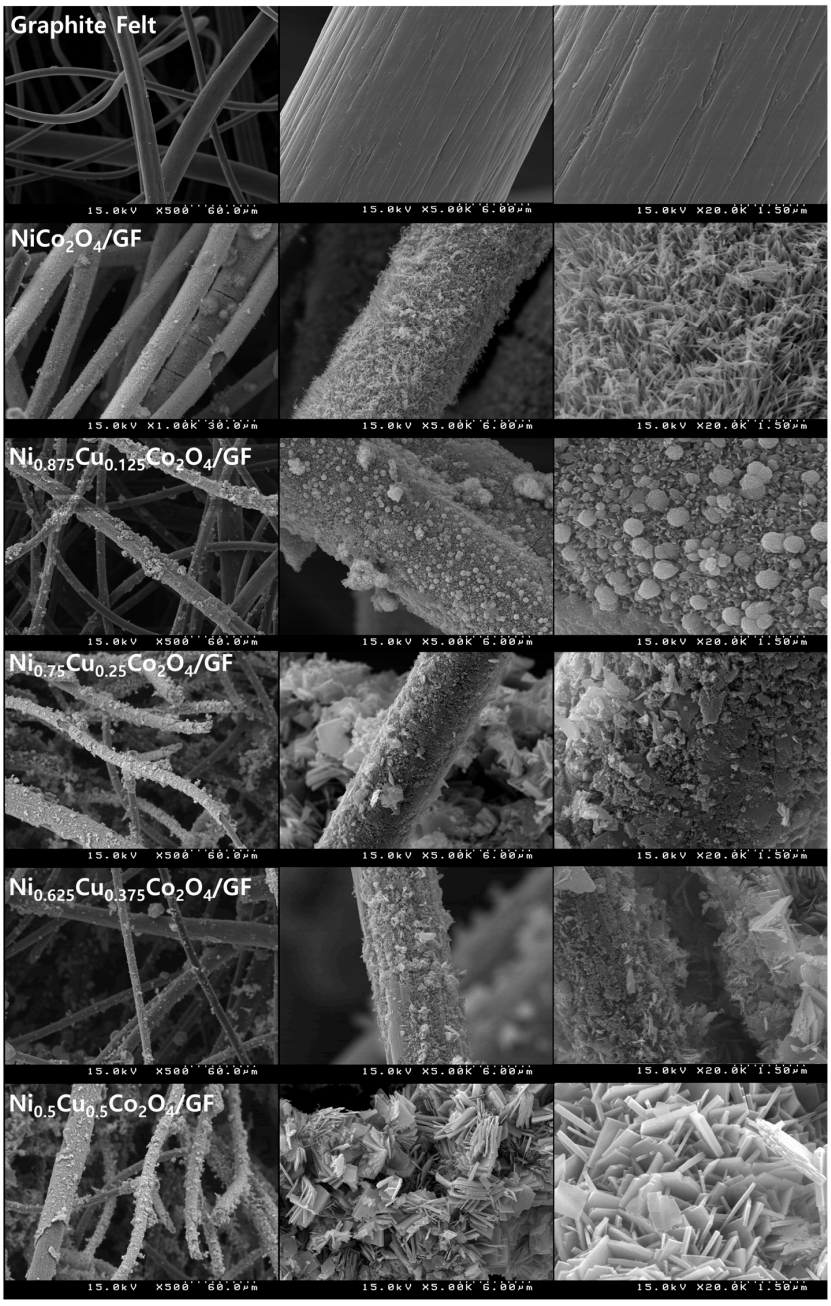

Figure 2. SEM images for the surfaces of $Ni_{1-x}Cu_xCo_2O_4$/GF electrodes.

Figure 3 shows the HR-TEM image, lattice fringe, SAED pattern, and element mapping image, which measured and dispersing it in ethanol solvent after scraping off the $Ni_{0.75}Cu_{0.25}Co_2O_4$ electrode active materials grown on the support electrode surface. Figure 3a shows the image of the dispersed $Ni_{0.75}Cu_{0.25}Co_2O_4$ particles. The particle size could not be confirmed clearly in the SEM photograph of Figure 2, but in the HR-TEM photograph, it was confirmed that the $Ni_{0.75}Cu_{0.25}Co_2O_4$ was composed of very small nanocrystals, and the size was about 10–20 nm. Figure 3b shows the lattice fringes in the selected area. The most clearly visible grating is a (220) facet having an interplane distance of 2.87 Å, a characteristic surface of the spinel structure [34]. Figure 3c shows the SAED (selected area diffraction) pattern at the same point as Figure 3a. The reciprocal of the distance from the center to the spot corresponds to the distance between the lattices, and (111), (220), (311), (400), and (511) facets were identified. It was found that $Ni_{0.75}Cu_{0.25}Co_2O_4$ particles are polycrystals in which various single crystals are mixed in various orientations [35]. In Figure 3d, the composed elementals in $Ni_{0.75}Cu_{0.25}Co_2O_4$ particle were confirmed by the STEM-element mapping image analysis, and the intensity of the color is proportional to the element concentration. Elements were evenly distributed on the particles, and no entangled elements were visible. Table 1 shows the atomic composition of the elements present in the assembled electrodes. The component concentrations present in most of the electrodes were almost stoichiometrically similar to the amount added during the preparing process. In particular, the atomic ratio of the constituent elements was Ni:Cu:Co:O = 10.3(3.1):3.2(1.0):28.0(8.8):59.9(18.7), which was almost quantitatively consistent with the molar ratio of the atoms (Ni:Cu:Co:O = 3:1:8:16) of the synthesized $Ni_{0.75}Cu_{0.25}Co_2O_4$ particles.

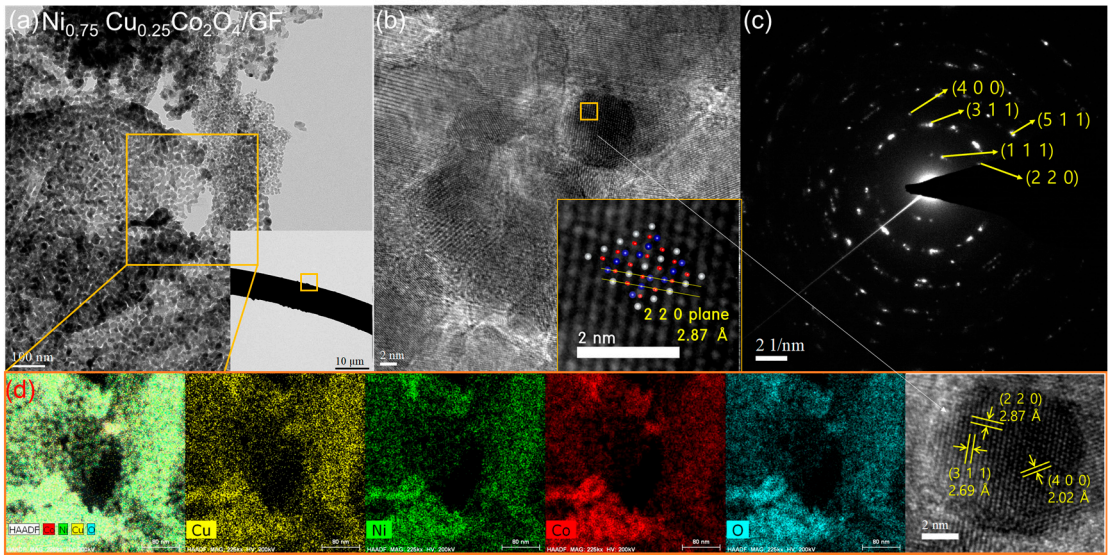

Figure 3. TEM image of $Ni_{0.75}Cu_{0.25}Co_2O_4$/GF electrode (**a**), HR-TEM images of the electrode surface (**b**), SAED patterns (**c**), and STEM-EDS mapping for all elements (**d**).

Table 1. Atomic compositions on $Ni_{1-x}Cu_xCo_2O_4$/GF electrodes obtained by the EDS analysis.

Sample \ Atomic (%)	Ni	Cu	Co	O	C
Graphite Felt	-	-	-	10.49	89.51
$NiCo_2O_4$/GF	7.46	-	14.88	29.82	47.84
$Ni_{0.875}Cu_{0.125}Co_2O_4$/GF	6.70	0.98	15.40	31.00	45.92
$Ni_{0.75}Cu_{0.25}Co_2O_4$/GF	5.51	1.70	14.98	32.11	45.70
$Ni_{0.625}Cu_{0.375}Co_2O_4$/GF	4.59	2.74	14.62	29.27	48.78
$NiCuCo_2O_4$/GF	3.93	3.52	14.83	29.64	48.08

3.2. Electrochemical Properties of $Ni_{1-x}Cu_xCo_2O_4$ Electrode Active Materials Grown on GF

Among the properties of catalysts used for electrochemical water decomposition, one of the important factors is the high electrochemically active surface area (ECSA) [36]. To predict ECSA, cyclic voltammetry (CV) was measured by varying the scan rate in the potential range of the non-faradaic region, and the current densities as a function of potential are plotted in Figure 4. In general, the rectangular shape of CV curve mean electrolyte ions accumulated on the electrode surface (electric double layer formation), indicating pure capacitive energy storage. When the redox current density is large in the same voltage range, the electroactive capacity is also large [37]. As the CV cycle increased, the redox current density in all samples increased. The redox current density increased as Cu was substituted, and it was found that the current density of $Ni_{0.75}Cu_{0.25}Co_2O_4$ increased drastically when the redox reactions occurred.

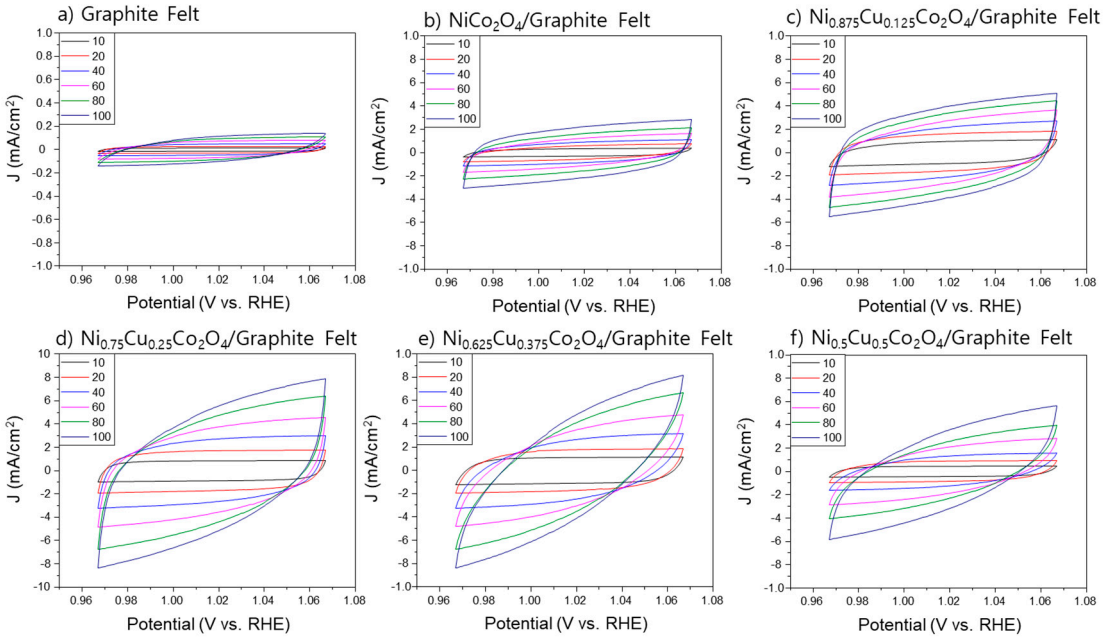

Figure 4. Cyclic voltammetry with scan rates in the non-faradaic region for all electrodes.

The current density differences (Janodic–Jcathodic, ΔJ) in all of electrodes are shown in Figure 5. The linear trend line slope was plotted with the values obtained in Figure 4 to measure the double layer capacitance (C_{dl}, double-layer capacitance, ESCA) and compared. The C_{dl} of GF calculated from the slope was calculated to be 21.2 mF cm^{-2}, and the C_{dl} value increased as a whole in the electrode active material coated on the GF surface. Especially for $Ni_{0.75}Cu_{0.25}Co_2O_4$/GF showed the highest ECSA value of 97.6 mF cm^{-2}, compared to the electrodes of $NiCo_2O_4$/GF (39.6 mF cm^{-2}), $Ni_{0.875}Cu_{0.125}Co_2O_4$/GF (62.8 mF cm^{-2}), $Ni_{0.625}Cu_{0.375}Co_2O_4$/GF (71.8 mF cm^{-2}), and $Ni_{0.5}Cu_{0.5}Co_2O_4$/GF (61.9 mF cm^{-2}). From these results, we predicted that $Ni_{0.75}Cu_{0.25}Co_2O_4$/GF will show a higher catalytically active site and will show excellent electrochemical catalyst performance [38].

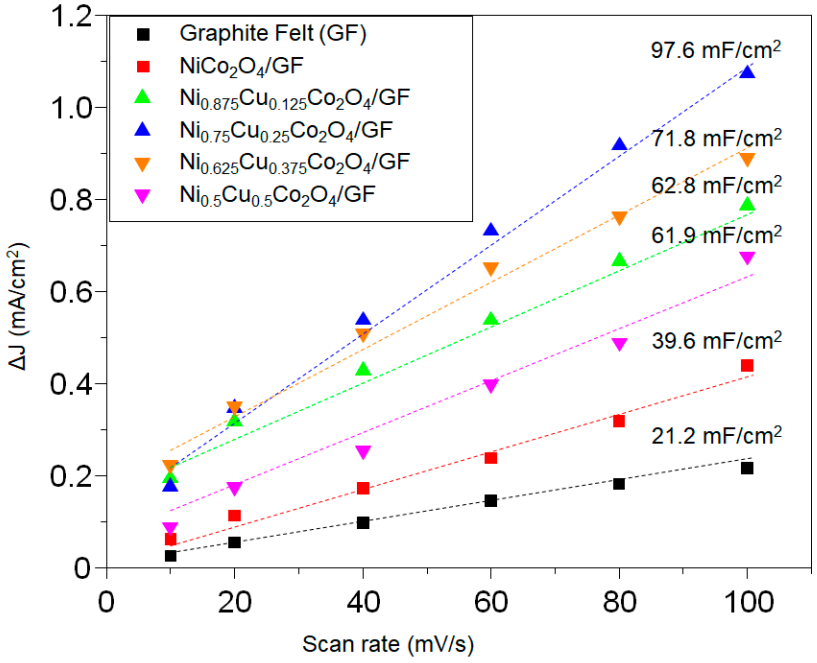

Figure 5. Current density differences depending on scan rate for all electrodes.

To compare the OER activity of the electrodes, LSV (linear scan voltammetry) curves were measured for all electrodes, and the results are shown in Figure 6a. In general, the electrolytic reaction describes the OER reactivity of the electrode by comparing the electrode potential at a current density of 10 mA cm^{-2} [39]. In order to reach a current density of 10 mA cm^{-2} at the GF support electrode, an overvoltage of 1.87 V is required. In $Ni_{1-x}Cu_xCo_2O_4$/GF electrodes, electrode potentials were obtained with 1.81 (η = 575 mV), 1.76 (η = 533 mV), 1.74 (η = 509 mV), 1.75 (η = 521 mV), and 1.79 V (η = 548 mV) in $NiCo_2O_4$/GF, $Ni_{0.875}Cu_{0.125}Co_2O_4$/GF, $Ni_{0.75}Cu_{0.25}Co_2O_4$/GF, $Ni_{0.625}Cu_{0.375}Co_2O_4$/GF, and $Ni_{0.5}Cu_{0.5}Co_2O_4$/GF electrodes, respectively. In particular, the $Ni_{0.75}Cu_{0.25}Co_2O_4$/GF electrode showed the lowest electrode potential, which means that it shows the best OER activity. Figure 6b shows the Tafel slope value derived from the LSV curve, and the Tafel slope shows the unique properties of the electrochemical catalytic electrode. The Tafel slope is the value of the electrode potential required when 10-fold electrons flow, and it is reported that the lower this value, the better the water-oxidation kinetics [40]. In Figure 6b, the Tafel slope of GF showed 325 mV dec^{-1}, and the $Ni_{0.75}Cu_{0.25}Co_2O_4$/GF electrode, which expressed the lowest electrode potential in the LSV curve, also showed the lowest Tafel slope with 119 mV dec^{-1}. For the $NiCo_2O_4$/GF electrode 173 mV dec^{-1}, 154 mV dec^{-1} for the $Ni_{0.875}Cu_{0.125}Co_2O_4$/GF electrode, 125 mV dec^{-1} for $Ni_{0.625}Cu_{0.375}Co_2O_4$/GF electrode, and 158 mV dec^{-1} for $Ni_{0.5}Cu_{0.5}Co_2O_4$/GF electrode were respectively obtained. These values were consistent with OER performance. Table 2 summarizes and compares the results of using noble or non-noble metal electrodes to recognize whether the electrochemical performance of $Ni_{1-x}Cu_xCo_2O_4$ electrode is high or low. The overpotential was widely distributed from 241 to 540 mV, and the Tafel values were also varied from 53 to 238 mV dec^{-1}. When nickel foam was used as a support electrode, the electrochemical performance was relatively excellent, whereas when a carbon electrode was used, it was significantly reduced. This is because the carbon electrode has a lower conductivity than the metal electrode. In addition, the performances vary depending on the shapes of graphite, but it is confirmed that the electrochemical performance was slightly lower than when using other carbon support electrodes because electrolyte wettability was lowered when GF was used. In the end, the performance in this study using GF was not largely improved in this reason.

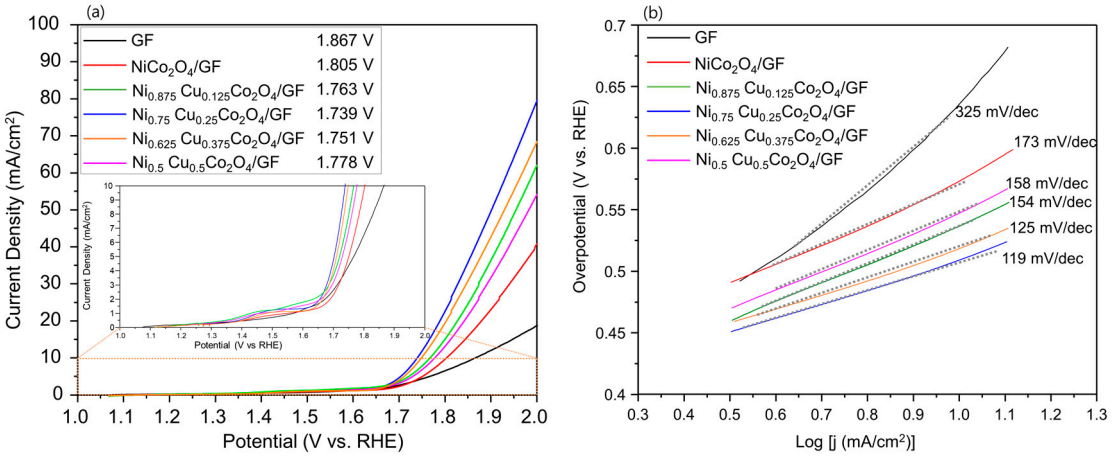

Figure 6. Linear scan voltammetry (LSV) curves for oxygen evolution reaction (OER) polarization of $Ni_{1-x}Cu_xCo_2O_4$/GF (**a**) and Tafel plots (**b**).

Table 2. Comparison of electrochemical performances for noble or non-noble metal electrodes.

Sample	Support	Overpotential (j = 10 mA cm^{-2})	Tafel Slope (mV dec^{-1})	Ref.
$Ni_{0.75}Cu_{0.25}Co_2O_4$	Graphite Felt	509 mV	119	This work
Co-P	Graphite Felt	530 mV (j = 5 mA cm^{-2})	133	[41]
CuS/$CuFeS_2$	Carbon Felt	400 mV	171	[42]
NiCu(I)	Ni foam	252 mV	54	[43]
$NiFe_2O_4$	Ni plate	520 mV	223	[44]
$CuFe_2O_4$	Ni plate	540 mV	238	[44]
Fe-Co$(OH)_2$	Glassy Carbon	290 mV	69	[45]
$NiCo_2S_4$/RGO	Glassy Carbon	366 mV	65	[46]
$NiCo_2O_4$/CoN_x-NMC NMC (Nitrogen doped Mesoporous Carbon)	Glassy Carbon	370 mV	99	[47]
$(Co_{0.21}Ni_{0.25}Cu_{0.54})_3Se_2$	Glassy Carbon	241 mV	53	[48]
FeCoNi alloy	N-doped graphene	288 mV	57	[49]
RuO_2	Glassy Carbon	300 mV	54	[49]
IrO_2	Glassy Carbon	314 mV	-	[50]

Electrochemical impedance spectroscopy (EIS) was performed to investigate the charge transfer properties of the electrode, in Figure 7. Generally, the size of the semicircle of the Nyquist plot is assigned to the charge transfer resistance (R_{ct}) [51]. Table 3 shows the R_s (solution resistance) and R_{ct} values for all of electrodes. The R_{ct} value was found to be 10.39 Ω, which was the highest value in the support electrode GF, and greatly decreased to 1.814 Ω in the $NiCo_2O_4$/GF electrode. Particularly, in the electrode substituted with 0.25 mol of Cu, the size of the electrode active material was reduced, and they were thinly and evenly grown on the electrode surface, and eventually the charge transfer resistance was significantly reduced to 0.728 Ω in the $Ni_{0.75}Cu_{0.25}Co_2O_4$/GF electrode. However, when Cu was replaced with more than that, the size of the electrode active material increased and the thickness of the plate-like particles thickened. As a result, the active area of the electrode surface decreased, and eventually the charge transfer resistance increased again to 1.631 Ω in the $Ni_{0.5}Cu_{0.5}Co_2O_4$/GF electrode.

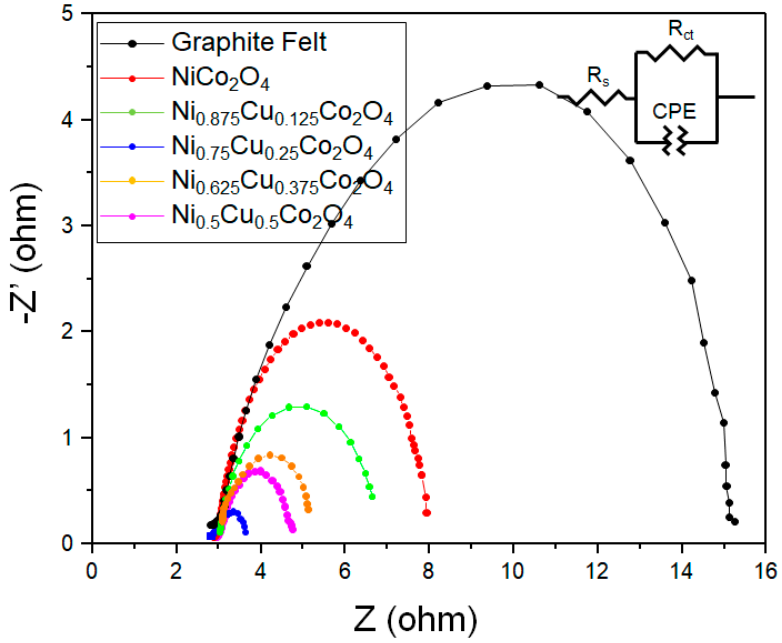

Figure 7. Nyquist plots for all electrodes under an applied potential of 1.7 V.

Table 3. Resistance behavior for all electrodes.

Factor \ Sample	Graphite Felt	$NiCo_2O_4$	$Ni_{0.875}Cu_{0.125}Co_2O_4$	$Ni_{0.75}Cu_{0.25}Co_2O_4$	$Ni_{0.625}Cu_{0.375}Co_2O_4$	$Ni_{0.5}Cu_{0.5}Co_2O_4$
R_S (Ω) (Solution Resistance)	2.960	2.768	2.627	2.654	2.613	3.012
R_{ct} (Ω) (Charge Transfer Resistance)	10.39	1.814	1.250	0.728	1.613	1.631
Total resistance (Ω)	13.35	4.582	3.877	3.382	4.226	4.643

3.3. Evaluation of the Durability of the Electrode

The long-term durability of the electrode serves as an important factor in evaluating the electrochemical material [52]. The stability of all electrodes was evaluated by applying a current of 10 mA cm^{-2} through chronopotentiometry for a total of 10 h, and the results are shown in Figure 8A. In the electrode coated with the electrode active material, the potential was maintained stably over time, but the GF support electrode showed an unstable potential until about 2 h, and it can be seen that the overpotential greatly increased after that. This can be attributed to the oxidization of the surface of the GF by continuous reaction [53]. Figure 8B shows the results for 100 h to further confirm the long-term stability of the $Ni_{0.75}Cu_{0.25}Co_2O_4$/GF electrode, which showed the highest performance. The initial stable voltage was maintained, and there was no significant difference in potential even after 100 h of reaction. It is judged that in the electrode coated with the electrode active material containing Cu, the OH^- intermediate formed on the electrode surface was rapidly oxidized by oxygen to suppress oxidation of the electrode surface, and as a result, a stable performance could be maintained [54]. Continuous accelerated stability testing is an important factor in evaluating the durability of the OER. Thus, the LSV curves for 1000 cycles at the $Ni_{0.75}Cu_{0.25}Co_2O_4$/GF electrode are presented in Figure 8C. Up to 300 cycles, the OER performance was rather improved, and gradually decreased from 400 cycles, but there was little change in performance from 700 cycles. This result means that the partial introduction of Cu into the lattice of $NiCo_2O_4$ not only improves the electrochemical performance of $NiCo_2O_4$, but also has a pretty positive effect on stability.

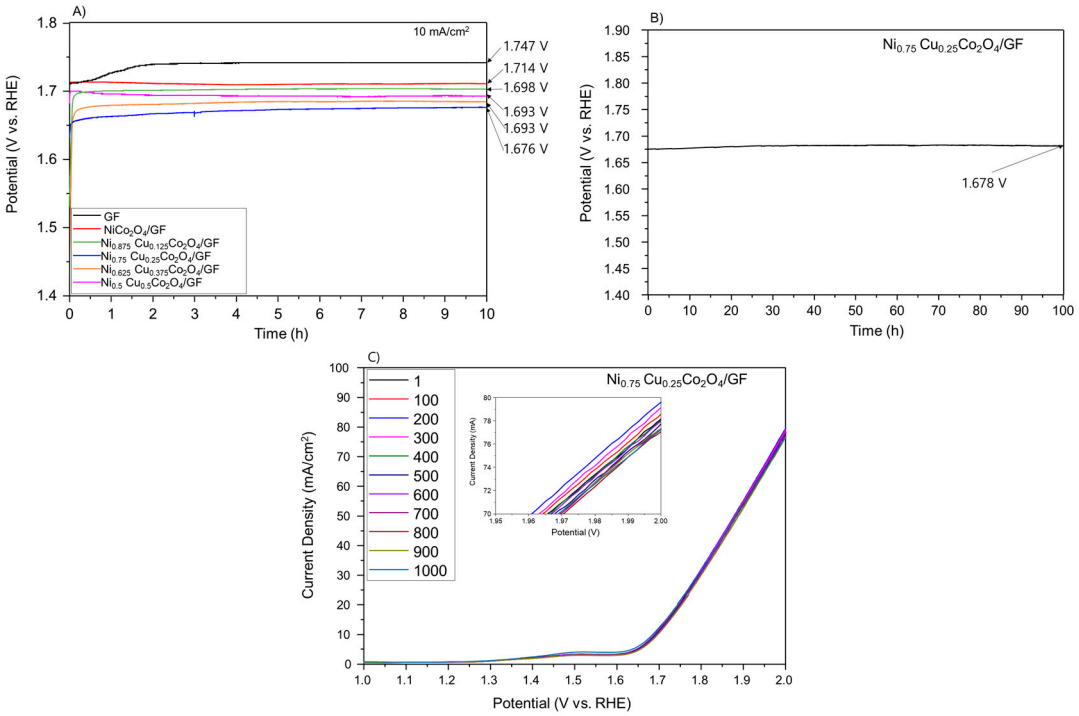

Figure 8. Chronopotentiometry of all electrodes for 10 h at 10 mA cm^{-2} (**A**), Chronopotentiometry for 100 h on the $Ni_{0.75}Cu_{0.25}Co_2O_4$/GF electrode (**B**), and 1000th cycled LSV curves for the $Ni_{0.75}Cu_{0.25}Co_2O_4$/GF electrode (**C**).

In order to know the difference between the actual efficiency and the theoretical efficiency of the $Ni_{0.75}Cu_{0.25}Co_2O_4$/GF electrode, an OER electrolysis reaction was performed while applying a current of 10 mA cm^{-2} for 4 h. At this time, the amount of oxygen generated was measured, and the theoretically calculated amount was compared with the actually generated amount. The theoretically calculated amount of oxygen was calculated using the following equation from Faraday's law [55].

$$n_{O_2}(\text{theoretical}) = \frac{Q}{nF} = \frac{I \times t}{nF} = \frac{0.01\ \text{A} \times 14400\ \text{s}}{4 \times 96485.3\ \text{s·A·mol}^{-1}} = 3.73 \times 10^{-4}\ \text{mol} \quad (2)$$

where n_{O_2} is the theoretically calculated amount of O_2, Q is the amount of applied charge, n is the number of electrons participating in the OER reaction (4 electrons), F is the Faraday constant (96485.3 s A mol^{-1}), i is the applied current (0.01 A), and t is the reaction time (14,400 s). Faraday efficiency is calculated using the following equation.

$$Faradaic\ efficiency = \frac{n_{O_2}(\text{measured})}{n_{O_2}(\text{theoretical})} \quad (3)$$

As a result of calculation, the Faraday efficiency of about 94.3% was exhibited at the $Ni_{0.75}Cu_{0.25}Co_2O_4$/GF electrode as shown in Figure 9, and this value means that almost all of the applied electrons were used for the oxygenation reaction without other side reactions except for experimental error.

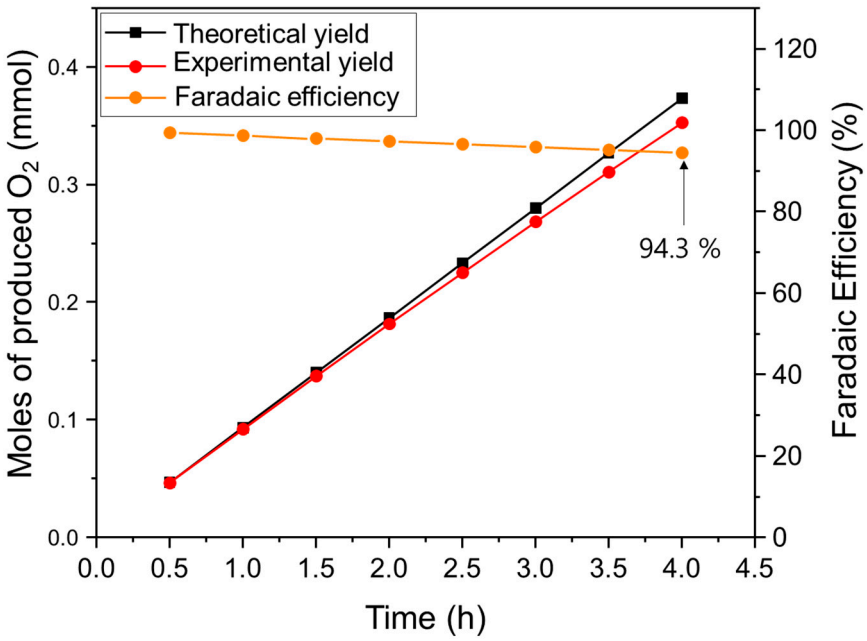

Figure 9. Faradaic efficiency of $Ni_{0.75}Cu_{0.25}Co_2O_4$/GF for the theoretically calculated and experimentally measured O_2 at a current density of 10 mA cm^{-2}.

In order to confirm the change in the oxidation state of the active elements after the 1000th OER cycle in the $Ni_{0.75}Cu_{0.25}Co_2O_4$/GF electrode showing the best performance, Figure 10A shows the XPS results before and after the OER reaction in the $Ni_{0.75}Cu_{0.25}Co_2O_4$/GF electrode. In addition, the XPS result before the OER reaction in the $NiCo_2O_4$/GF electrode was compared with those. At the $Ni_{0.75}Cu_{0.25}Co_2O_4$/GF electrode before the OER reaction, peaks which corresponding to $2p_{3/2}$ and $2p_{1/2}$ electron spins of Cu^{2+} were identified at 934.1 eV and 954.0 eV, respectively [56]. The difference in the separated binding energy was 19.9 eV, similar to the value reported in the literature, 19.8 eV [57]. In addition, a satellite peak was appeared at 940–943 eV, which is a peak caused by the transfer of 3d electrons (d–d transfer) between the metal and the ligand, and is a major factor in confirming the presence of Cu^{2+} [58]. In the electrode after the reaction, the peaks of Cu $2p_{3/2}$ and Cu $2p_{1/2}$ shifted to 933.4 eV and 953.4 eV, respectively. We were convinced from the slight decrease in the binding energy after the 1000th OER reaction that Cu^{2+} ions were attracted the electrons, which emitted by oxidation of OH^- ions during the OER reaction. This is probably evidence that the evolution of oxygen in the spinel lattice occurs at the oxygen site linked to Cu^{2+}. That is, as Cu^{2+}, which has a higher potential than Ni^{2+} and Co^{2+}, is spontaneously reduced, oxygen vacancies are formed around it, and the vacancies easily adsorbed water or OH^-, which in turn improves OER performance. In the Ni 2p XPS spectrum of the $NiCo_2O_4$/GF electrode, peaks that correspond to Ni^{2+} $2p_{3/2}$, Ni^{3+} $2p_{3/2}$, Ni^{2+} $2p_{1/2}$, and Ni^{3+} $2p_{1/2}$ appeared respectively at the binding energies of 854.9, 857.0, 872.2, and 874.8 eV [59]. In the Ni 2p XPS spectra of the Cu-containing $Ni_{0.75}Cu_{0.25}Co_2O_4$/GF electrode, they were found at 855.2, 857.3, 872.4, and 874.8 eV, respectively. As Cu was introduced, the binding energy of Ni moved to the slightly higher (Ni^{3+}). This is because some of the Ni^{2+} present in the tetrahedral site moves to the octahedral site by the introduction of Cu and forms a stronger bond with oxygen [60]. In the spectrum of the $Ni_{0.75}Cu_{0.25}Co_2O_4$/GF electrode after the OER reaction, peaks were observed at 855.1, 856.8, 872.1, and 874.4 eV, respectively. This is a decrease of about 0.1–0.4 eV from the binding energy before the reaction. Moreover, the area of the peak of Ni^{2+} increased significantly compared to that before the reaction, which means that Ni^{3+} (maybe NiOOH) is being reduced to Ni^{2+} during the OER reaction. In the Co 2p XPS spectrum of $NiCo_2O_4$/GF, peaks corresponding to Co^{3+} $2p_{3/2}$, Co^{2+} $2p_{3/2}$, Co^{3+} $2p_{1/2}$, and Co^{2+} $2p_{1/2}$ were identified at 779.1, 780.3, 794.1, and 795.6 eV, respectively. From this result, we were convinced that Co^{3+} and Co^{2+} coexisted in this sample [61]. As Cu^{2+} was introduced,

Co^{2+} present in the Td site was oxidized to Co^{3+} while moving to the Oh site, so the proportion of Co^{3+} increased [62]. Therefore, the peaks at the $Ni_{0.75}Cu_{0.25}Co_2O_4$/GF electrode before the reaction appeared at 779.8, 780.9, 794.8, and 796.3 eV, and these shifted to a higher binding energy of about 0.3–0.7 eV compared to the $NiCo_2O_4$/GF electrode. In the $Ni_{0.75}Cu_{0.25}Co_2O_4$/GF electrode after the reaction, these peaks shifted to slightly higher binding energies of 780.1, 781.2, 795.1, and 796.4 eV, respectively. However, the shift was too small. This means that CoOOH was changed to Co_2O_3 rather than a change from Co_2O_3 to CoO during the OER reaction. For O 1s in the $NiCo_2O_4$/GF electrode, peaks corresponding to M-O, oxygen defects and M-OH, and physically adsorbed H_2O were identified at 529.4, 531.2, and 533.1 eV, respectively [63]. As Cu was introduced, the peak areas for M-O and M-OH were greatly increased. This means that oxygen defects have already occurred in the spinel lattice due to the introduction of copper before the OER reaction. In the $Ni_{0.75}Cu_{0.25}Co_2O_4$/GF electrode after the OER reaction, the area of peaks for M-OH and C=O-OH increased over a wide range. This is predictable evidence that oxygen vacancies are formed in the lattice due to the introduction of Cu, and that OH^- is easily adsorbed to the defect sites. Figure 10B shows the overall reaction cycle of the OER reaction occurring on the electrode surface. From the stepwise reactions occurring at the interface between the active material of the electrode and the electrolyte during the OER reaction, we can recognize a series of processes in which O_2 and electrons are generated as the $4OH^-$ ions in the electrolyte are oxidized. In addition, through this cycle, it was confirmed that the oxidation–reduction processes of active metals were consistent with XPS results.

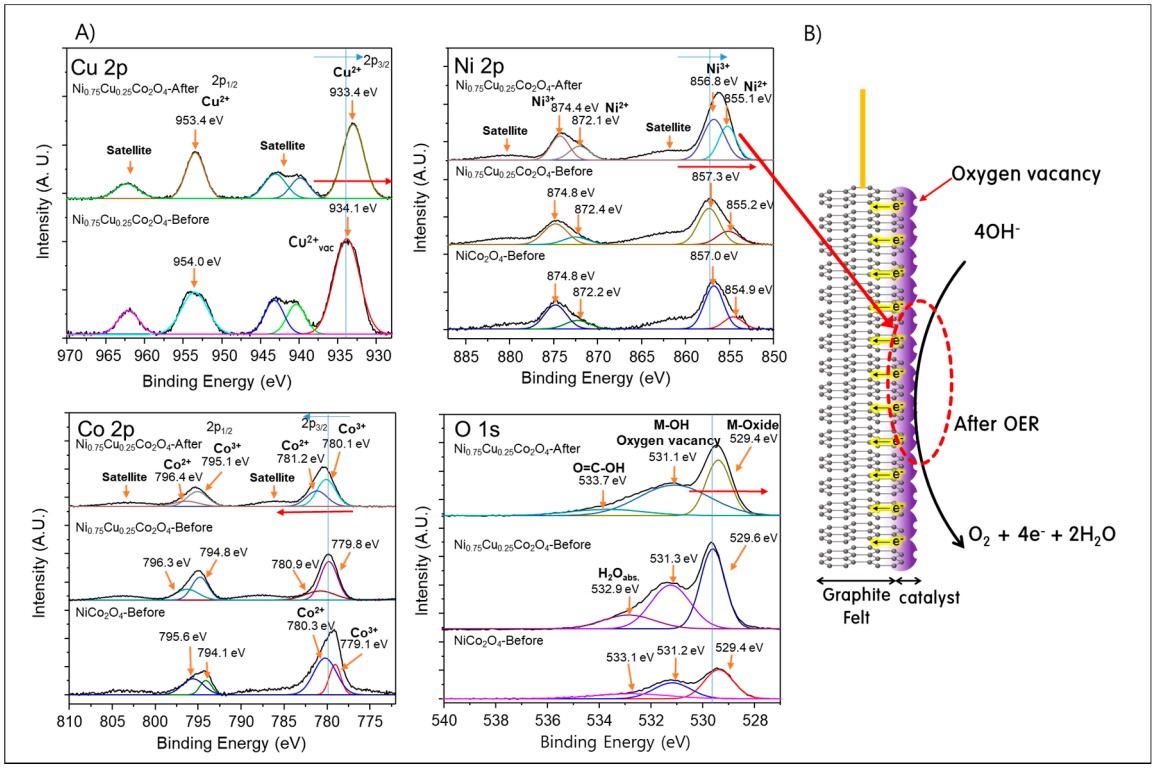

Figure 10. XPS spectra for the $NiCo_2O_4$ electrode (**A**) and surface phenomena on the $Ni_{0.75}Cu_{0.25}Co_2O_4$/GF electrode before and after the OER reaction (**B**).

Based on the above results, the mechanism of the predictable OER reaction was expressed in Scheme 2, and the OER mechanism occurring in the basic solution is simplified as follows [64].

$$M + OH^- \rightarrow M\text{-}OH \quad (4)$$

$$MOH + OH^- \rightarrow MO + H_2O\ (l) \quad (5)$$

$$2MO \rightarrow 2M + O_2(g) \quad (6)$$

$$MO + OH^- \rightarrow MOOH + e^- \quad (7)$$

$$MOOH + OH^- \rightarrow M + O_2(g) + H_2O\ (l) \quad (8)$$

$$\text{Overall reaction: } M + 4OH^- \rightarrow M + O_2\ (g) + 2H_2O + 4e^- \quad (9)$$

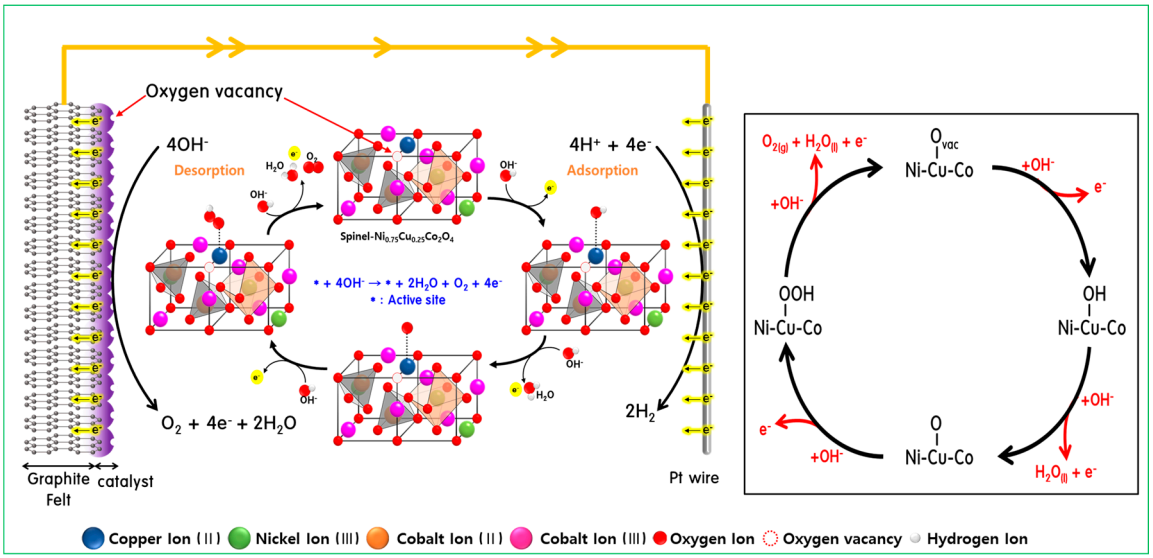

Scheme 2. Mechanism of OER on the surface $Ni_{0.75}Cu_{0.25}Co_2O_4$/GF electrode in alkaline solution.

First, with the introduction of Cu^{2+}, oxygen vacancies were formed in the $Ni_{1-x}Cu_xCo_2O_4$ (or Ni-Cu-Co-O_{vac}) spinel structure due to the relative redox potential difference between Cu^{2+}, Ni^{2+}, and Co^{2+}. In the first step reaction, OH^- ions in the electrolyte were adsorbed to oxygen vacancies formed on the surface of the material, generating one electron, and the Ni-Cu-Co-O_{vac} surface becomes (Ni-Cu-Co)-OH. In the second step, H_2O was generated while another OH^- ion of the electrolyte removed H^+ ions bound to the material, and one electron was generated and the material surface became (Ni-Cu-Co)-O. In the third step, another OH^- ion of the electrolyte was bonded to O on the material surface to become (Ni-Cu-Co)-OOH, and one electron was generated. Finally, in the fourth step, another OH^- ion in the electrolyte removed H^+ from the -OOH group on the surface of (Ni-Cu-Co)-OOH, resulting in H_2O, and one electron was generated. At this time, the remaining -OO was also dissociated to O_2, and the material returned to the initial state of Ni-Cu-Co-O_{vac}. The four electrons generated during the OER reaction were transferred to the GF collector layer and then discharged to the HER electrode through an external circuit.

4. Conclusions

For an efficient and stable OER reaction, an OER electrode was prepared by growing a $Ni_{1-x}Cu_xCo_2O_4$ electrode active material on a GF support electrode through hydrothermal synthesis. The pure GF support electrode not only had low performance but also tended to be easily oxidized, but through the method of growing the electrode active material on the surface, it was possible to increase the surface active site and increase the electrode stability for a long time. XRD, SEM, and TEM image analysis was confirmed, showing the change in crystallinity and shape as Cu was partially introduced into the $NiCo_2O_4$ spinel structure. As a result of carrying out a water decomposition OER reaction in 1.0 M KOH alkaline electrolyte, the Tafel value of 325 mV dec^{-1} was found in the GF electrode, but was significantly improved to 119 mV dec^{-1} in the $Ni_{0.75}Cu_{0.25}Co_2O_4$/GF electrode. In addition, the $Ni_{0.75}Cu_{0.25}Co_2O_4$/GF electrode exhibited a Faraday efficiency of 94.3% and was confirmed to have a high catalytically active surface area of 97.6 mF cm^{-2}. Moreover, the activity

was maintained without deterioration even after a long time reaction of more than 1000th cycles. In conclusion, in this study, the adsorption of OH^- ions was facilitated through oxygen vacancies caused by the introduction of Cu, and it is considered that the performance was maintained even in long-term reactions.

Author Contributions: Conceptualization: H.P., S.K.; methodology: B.H.P., J.C.; investigation: H.P., T.K.; writing—original draft preparation: N.S.; writing—review and editing: M.K.; visualization: N.S.; supervision: J.H.K., Y.-S.Y.; project administration: M.K. All authors have read and agreed to the published version of the manuscript.

Funding: This research was funded by a Yeungnam University research grant 2019 (Grant No. 219A345005) and X-mind Corps program of National Research Foundation of Korea (NRF) funded by the Ministry of Science, ICT (2019H1D8A110563011).

Conflicts of Interest: The authors declare no conflict of interest.

References

1. Cobo, S.; Heidkamp, J.; Jacques, P.A.; Fize, J.; Fourmond, V.; Guetaz, L.; Jousselme, B.; Ivanova, V.; Dau, H.; Palacin, S.; et al. A Janus cobalt-based catalytic material for electro-splitting of water. *Nat. Mater.* **2012**, *11*, 802–807. [CrossRef] [PubMed]
2. Zhou, H.; Yu, F.; Zhu, Q.; Sun, J.; Qin, F.; Yu, L.; Bao, J.; Yu, Y.; Chen, S.; Ren, Z. Water splitting by electrolysis at high current densities under 1.6 volts. *Energy Environ. Sci.* **2018**, *11*, 2858–2864. [CrossRef]
3. Bizzotto, F.; Quinson, J.; Zana, A.; Kirkensgaard, J.J.K.; Dworzak, A.; Oezaslan, M.; Arenz, M. Ir nanoparticles with ultrahigh dispersion as oxygen evolution reaction (OER) catalysts: Synthesis and activity benchmarking. *Catal. Sci. Technol.* **2019**, *9*, 6345–6356. [CrossRef]
4. Yi, J.; Lee, W.H.; Choi, C.H.; Lee, Y.; Park, K.S.; Min, B.K.; Hwang, Y.J.; Oh, H.S. Effect of Pt introduced on Ru-based electrocatalyst for oxygen evolution activity and stability. *Electrochem Commun.* **2019**, *104*, 106469. [CrossRef]
5. Markoulaki, V.I.; Papadas, I.T.; Kornarakis, I.; Armatas, G.S. Synthesis of Ordered Mesoporous CuO/CeO_2 Composite Frameworks as Anode Catalysts for Water Oxidation. *Nanomaterials* **2015**, *5*, 1971–1984. [CrossRef] [PubMed]
6. Liu, R.; Wang, Y.; Liu, D.; Zou, Y.; Wang, S. Water-Plasma-Enabled Exfliation of Ultrathin Layered Double Hydroxide Nanosheets with Multivacancies for Water Oxidation. *Adv. Mater.* **2017**, *29*, 1701546. [CrossRef] [PubMed]
7. Man, H.W.; Tsang, C.S.; Li, M.M.J.; Mo, J.; Huang, B.; Lee, L.Y.S.; Leung, Y.C.; Wong, K.Y.; Tsang, S.C.E. Tailored transition metal-doped nickel phosphide nanoparticles for the electrochemical oxygen evolution reaction (OER). *Chem. Commun.* **2018**, *54*, 8630–8633. [CrossRef]
8. He, F.; Wu, L.; Wei, G.; Zhang, H.; Yan, J. Electrical conductivity and ion transfer behavior of $NiCo_2O_4$ with different micro structures. *Results Phys.* **2020**, *16*, 102875. [CrossRef]
9. Finger, L.W.; Hazen, R.M.; Hofmeister, A.M. High-Pressure Crystal Chemistry of Spinel ($MgAl_2O_4$) and Magnetite (Fe_3O_4): Conparisons with Silicate Spinels. *Phys. Chem. Miner.* **1986**, *13*, 215–220. [CrossRef]
10. Kumari, P.; Sharma, K.; Pal, P.; Kumar, M.; Ichikawa, T.; Jain, A. highly efficient & stable Bi & Sb anodes using lithium borohydride as solid electrolyte in Li-ion batteries. *RSC Adv.* **2019**, *9*, 13077–13081.
11. Chen, Y.; Ji, S.; Zhao, S.; Chen, W.; Dong, J.; Cheong, W.C.; Shen, R.; Wen, X.; Zheng, L.; Rykov, A.I.; et al. Enhanced oxygen reduction with single-atomic-site iron catalysts for a zinc-air vattery and hydrogen-air fuel cell. *Nat. Commun.* **2018**, *9*, 5422. [CrossRef] [PubMed]
12. Jung, H.G.; Hassoun, J.; Park, J.B.; Sun, Y.K.; Scrosati, B. An improved high-performance lithium-air battery. *Nat. Chem.* **2012**, *4*, 579–585. [CrossRef] [PubMed]
13. Chen, R.; Wang, H.Y.; Miao, J.; Yang, H.; Liu, B. A flexible high-performance oxygen evolution electrode with three-dimensional $NiCo_2O_4$ core-shell nanowires. *Nano Energy* **2015**, *11*, 333–340. [CrossRef]
14. An, L.; Huang, L.; Zhou, P.; Yin, J.; Liu, H.; Xi, P. A Self-Standing High-Performance Hydrogen Evolution Electrode with Nanostructured $NiCo_2O_4$/CuS Heterostructures. *Adv. Funct. Mater.* **2015**, *25*, 6814–6822. [CrossRef]

15. Hassan, D.; El-safty, S.; Khalil, K.A.; Dewidar, M.; El-magd, G.A. Carbon Supported Engineering $NiCo_2O_4$ Hybrid Nanofibers with Enhanced Electrocatalytic Activity for Oxygen Reduction Reaction. *Materials* **2016**, *9*, 759. [CrossRef]
16. Das, A.K.; Layek, R.K.; Kim, N.H.; Jung, D.; Lee, J.H. Reduced graphene oxide (RGO)-supported $NiCo_2O_4$ nanoparticles: An electrocatalyst for methanol oxidation. *Nanoscale* **2014**, *6*, 10657–10665. [CrossRef]
17. Yang, L.; Zhang, B.; Fang, B.; Feng, L. A comparative study of $NiCo_2O_4$ catalyst supported on Ni foam and from solution residuals fabricated by a hydrothermal approach for electrochemical oxygen evolution reaction. *Chem. Commun.* **2018**, *54*, 13151–13154. [CrossRef]
18. Tavares, A.C.; Cartaxo, M.A.M.; da Silva Pereira, M.I.; Costa, F.M. Effect of the partial replacement of Ni or Co by Cu on the electrocatalytic activity of the $NiCo_2O_4$ spinel oxide. *J. Electroanal. Chem.* **1999**, *464*, 187–197. [CrossRef]
19. Mugheri, A.Q.; Tahira, A.; Aftab, U.; Bhatti, A.L.; Memon, N.N.; Memon, J.R.; Abro, M.I.; Shah, A.A.; Willander, M.; Hullioa, A.A.; et al. Efficient tri-metallic oxides $NiCo_2O_4$/CuO for the oxygen evolution reaction. *RSC Adv.* **2019**, *9*, 42387–42394. [CrossRef]
20. Ezeigwe, E.R.; Khiew, P.S.; Siong, C.W.; Tan, M.T.T. Solvothermal synthesis of $NiCo_2O_4$ nanocomposites on liquid-phase exfoliated graphene as an electrode material for electrochemical capacitors. *J. Alloys Compd.* **2017**, *693*, 1133–1142. [CrossRef]
21. Chen, X.; Li, H.; Xu, J.; Jaber, F.; Musharavati, F.; Zalnezhad, E.; Bae, S.; Hui, K.S.; Hui, K.N.; Liu, J. Synthesis and Characterization of a $NiCo_2O_4$@$NiCo_2O_4$ Hierarchical Mesoporous Nanoflake Electrode for Supercapacitor Applications. *Nanomaterials* **2020**, *10*, 1292. [CrossRef]
22. Yan, A.L.; Wang, W.D.; Chen, W.Q.; Wang, X.C.; Liu, F.; Cheng, J.P. The Synthesis of $NiCo_2O_4$-MnO_2 Core-shell nanowires by Electrodeposition and Its Supercapacitive Properties. *Nanomaterials* **2019**, *9*, 1398. [CrossRef] [PubMed]
23. Han, X.; Gui, X.; Yi, T.F.; Li, Y.; Yue, C. Recent progress of $NiCo_2O_4$-based anodes for high-performance lithium-ion batteries. *Curr. Opin. Solid State Mater. Sci.* **2018**, *22*, 109–126. [CrossRef]
24. Laziz, N.A.; Rjeily, J.A.; Darwiche, A.; Toufaily, J.; Outzourhit, A.; Ghanouss, F.; Sougrati, M.T. Li- and Na-ion Storage Performance of Natural Graphite via Simple Flotation Process. *J. Electrochem. Sci. Technol.* **2018**, *9*, 320–329. [CrossRef]
25. Choi, S.K.; Choi, W.; Park, H. Solar water oxidation using nickel-borate coupled $BiVO_4$ photoelectrodes. *Phys. Chem. Chem. Phys.* **2013**, *15*, 6499–6507. [CrossRef] [PubMed]
26. Yuan, H.; Li, J.; Yang, W.; Zhuang, Z.; Zhao, Y.; He, L.; Xu, L.; Liao, X.; Zhu, R.; Mai, L. Oxygen Vacancy-Determined Highly Efficient Oxygen Reduction in $NiCo_2O_4$/Hollow Carbon Spheres. *ACS Appl. Mater. Interfaces* **2018**, *10*, 16410–16417. [CrossRef] [PubMed]
27. Li, N.; Ai, L.; Jiang, J.; Liu, S. Spinel-type oxygen-incorporated Ni^{3+} self-doped Ni_3S_4 ultrathin nanosheets for highly efficient and stable oxygen evolution electrocatalysis. *J. Colloid Interf. Sci.* **2020**, *564*, 418–427. [CrossRef]
28. Ivanenko, I.; Coronova, A.; Astrelin, I.; Romanenko, Y. Structural and catalytic properties of Ni-Co spinel and its conposites. *Bull. Mater. Sci.* **2019**, *42*, 172. [CrossRef]
29. Marco, J.F.; Gancedo, J.R.; Gracia, M. Characterization of the Nickel Cobaltite, $NiCo_2O_4$, Prepared by Several Methods: An XRD, XANES, EXAFS, and XPS Study. *J. Solid State Chem.* **2000**, *153*, 74–81. [CrossRef]
30. Feng, Y.; Liu, J.; Wub, D.; Zhou, Z.; Deng, Y.; Zhang, T.; Shih, K. Efficient degradation of sulfamethazine with $CuCo_2O_4$ spinel nanocatalysts for peroxymonosulfate activation. *Chem. Eng. J.* **2015**, *280*, 514–524. [CrossRef]
31. Do, J.Y.; Son, N.; Park, N.K.; Kwak, B.S.; Beak, J.I.; Ryu, H.J.; Kang, M. Reliable oxygen transfer in $MgAl_2O_4$ spinel through the reversible formation of oxygen vacancies by Cu^{2+}/Fe^{3+} anchoring. *Appl. Energy* **2018**, *219*, 138–150. [CrossRef]
32. Avaji, P.G.; Patil, S.A.; Badami, P.S. Synthesis, spectral, thermal, solid state d.c. electrical conductivity and biological studies of Co(II), Ni(II) and Cu(II) complexes with 3-substituted-4-amino (indole-3-aldehydo)-5-mercapto-1,2,4-triazole Schiff bases. *J. Coord. Chem.* **2008**, *61*, 1884–1896. [CrossRef]
33. Tsai, C.L.; Chou, B.; Cheng, S.; Lee, J.F. Synthesis of TMBQ using Cu(II)-substituted MCM-41 as the catalyst. *Appl. Catal. A-Gen.* **2001**, *208*, 279–289. [CrossRef]

34. Zhang, L.; Zhang, D.; Ren, Z.; Huo, M.; Dang, G.; Min, F.; Zhang, Q.; Xie, J. Mesoporous $NiCo_2O_4$ Micro/nanospheres with Hierarchical Structures for Supercapacitors and Methanol Electro–Oxidation. *Chem. Electro. Chem.* **2017**, *4*, 441–449.
35. Shanmugavel, T.; Raj, S.G.; Kumar, G.R.; Rajarajan, G.; Saravanan, D. Cost effective preparation and characterization of nanocrystalline nickel ferrites ($NiFe_2O_4$) in low temperature regime. *J. King Saud Univ. Sci.* **2015**, *27*, 176–181. [CrossRef]
36. Li, X.; Fang, Y.; Lin, X.; Tian, M.; An, X.; Fu, Y.; Li, R.; Jin, J.; Ma, J. MOF derived Co_3O_4 nanoparticles embedded in N-doped mesoporous carbon layer/MWCNT hybrids: Extraordinary bi-functional electrocatalysts for OER and ORR. *J. Mater. Chem. A* **2015**, *3*, 17392–17402. [CrossRef]
37. Anantharaj, S.; Ede, S.R.; Karthick, K.; Sankar, S.S.; Sangeetha, K.; Karthick, P.E.; Kundu, S. Precision and correctness in the evaluation of electrocatalytic water splitting: Revisiting activity parameters with a critical assessment. *Energy Environ. Sci.* **2018**, *11*, 744–771. [CrossRef]
38. He, J.; Guan, L.; Zhou, Y.; Shao, P.; Yao, Y.; Lu, S.; Kong, L.; Liao, X. One-pot preparation of mesoporous $K_xPMo_{12}O_{40}$ (x = 1, 2, 3, 4) materials for oxidative desulfurization: Electrochemically-active surface area (ECSA) determines their activity. *React. Chem. Eng.* **2020**, in press. [CrossRef]
39. Liu, T.; Asirib, A.M.; Sun, X. Electrodeposited Co-doped $NiSe_2$ nanoparticles film: A good electrocatalyst for efficient water splitting. *Nanoscale* **2016**, *8*, 3911–3915. [CrossRef]
40. Wu, P.; Wu, J.; Si, H.; Zhang, Z.; Liao, Q.; Wang, X.; Dai, F.; Ammarah, K.; Kang, Z.; Zhang, Y. 3D Holey-Graphene Architecture Expedites Ion Transport Kinetics to Push the OER Performance. *Adv. Energy Mater.* **2020**, *10*, 2001005. [CrossRef]
41. Liu, L.; Zhang, D.; Duan, D.; Li, Y.; Yuan, Q.; Chen, L.; Liu, S. In situ fabrication of 3D self-supporting cobalt phosphate-modified graphite felt electrocatalysts for oxygen evolution reaction in neutral solution. *J. Electroanal. Chem.* **2020**, *862*, 114031. [CrossRef]
42. Zang, N.; Wu, Z.; Wang, J.; Jin, W. Rational design of Cu-Co thiospinel ternary sheet arrays for highly efficient electrocatalytic water splitting. *J. Mater. Chem. A* **2020**, *8*, 1799–1807. [CrossRef]
43. Xie, Y.S.; Wang, Z.; Ju, M.; Long, X.; Yang, S. Dispersing transition metal vacancies in layered double hydroxides by ionic reductive complexation extraction for efficient water oxidation. *Chem. Sci.* **2019**, *10*, 8354–8359. [CrossRef] [PubMed]
44. Li, M.; Xiong, Y.; Liu, X.; Bo, X.; Zhang, Y.; Han, C.; Guo, L. Facile synthesis of electrospun MFe_2O_4 (M = Co, Ni, Cu, Mn) spinel nanofibers with excellent electrocatalytic properties for oxygen evolution and hydrogen peroxide reduction. *Nanoscale* **2015**, *7*, 8920–8930. [CrossRef]
45. Cao, B.; Luo, C.; Lao, J.; Chen, H.; Qi, R.; Lin, H.; Peng, H. Facile Synthesis of 3d Transition-Metal-Doped α-$Co(OH)_2$ Nanomaterials in Water−Methanol Mediated with Ammonia for Oxygen Evolution Reaction. *ACS Omega* **2019**, *4*, 16612–16618. [CrossRef]
46. Shuai, C.; Mo, Z.; Niu, X.; Yang, X.; Liu, G.; Wang, J.; Liu, N.; Guo, R. Hierarchical $NiCo_2S_4$ nanosheets grown on graphene to catalyze the oxygen evolution reaction. *J. Mater. Sci.* **2020**, *55*, 1627–1636. [CrossRef]
47. Qiao, M.F.; Wang, Y.; Li, L.; Hu, G.Z.; Zou, G.A.; Mamat, X.; Dong, Y.M.; Hu, X. Self-templated nitrogen-doped mesoporous carbon decorated with double transition-metal active sites for enhanced oxygen electrode catalysis. *Rare Met.* **2020**, *39*, 824–833. [CrossRef]
48. Cao, X.; Johnson, E.; Nath, M. Identifying high-efficiency oxygen evolution electrocatalysts from Co–Ni–Cu based selenides through combinatorial electrodeposition. *J. Mater. Chem. A* **2019**, *7*, 9877–9889. [CrossRef]
49. Shi, Q.; Fu, S.; Zhu, C.; Song, J.; Du, D.; Lin, Y. Metal-organic frameworks-based catalysts for electrochemical oxygen evolution. *Mater. Horiz.* **2019**, *6*, 684–702. [CrossRef]
50. Lee, H.; Kim, J.Y.; Lee, S.Y.; Hong, J.A.; Kim, N.; Baik, J.; Hwang, Y.J. Comparative study of catalytic activities among transition metal-doped IrO_2 nanoparticles. *Sci. Rep.* **2018**, *8*, 16777. [CrossRef]
51. Samant, S.; Bhuni, K.; Prandhan, D.; Satpati, B.; Srivastava, R. $NiCuCo_2O_4$ Supported Ni−Cu Ion-Exchanged Mesoporous Zeolite Heteronano Architecture: An Efficient, Stable, and Economical Nonprecious Electrocatalyst for Methanol Oxidation. *ACS Sustain. Chem. Eng.* **2018**, *6*, 2023–2036. [CrossRef]
52. Feng, B.; Liu, C.; Yan, W.; Geng, J.; Wang, G. MoS_2 nanotuves loaded with TiO_2 nanoparticles for enhanced electrocatalytic hydrogen evolution. *RSC Adv.* **2019**, *9*, 26487–26494. [CrossRef]
53. Yi, Y.; Weinberg, G.; Prenzel, M.; Greiner, M.; Heumann, S.; Becker, S.; Schlögl, R. Electrochemical corrosion of a glassy carbon electrode. *Catal. Today* **2017**, *295*, 32–40. [CrossRef]

54. Kusmierek, E. Evaluating the Effect of WO_3 on Electrochemical and Corrosion Properties of TiO_2-RuO_2-Coated Titanium Anodes with Low Content of RuO_2. *Electrocatalysis* **2020**, *11*, 555–566. [CrossRef]
55. Mosa, I.M.; Biswas, S.; El-Sawy, A.M.; Botu, V.; Guild, C.; Song, W.; Ramprasad, R.; Ruslingace, J.F.; Suib, S.L. Tunable mesoporous manganese oxide for high performance oxygen reduction and evolution reactions. *J. Mater. Chem. A* **2016**, *4*, 620–631. [CrossRef]
56. Monte, M.; Munuera, G.; Costa, D.; Conesa, J.C.; Arias, A.M. Near-ambient XPS characterization of interfacial copper species in ceria-supported copper catalysts. *Phys. Chem. Chem. Phys.* **2015**, *17*, 29995–30004. [CrossRef]
57. Amri, A.; Jiang, Z.T.; Zhao, X.; Xie, Z.; Yin, C.Y.; Ali, N.; Mondinos, N.; Rahman, M.M.; Habibi, D. Tailoring the physicochemical and mechanical properties of optical copper–cobalt oxide thin films through annealing treatment. *Surf. Coat. Technol.* **2014**, *239*, 212–221. [CrossRef]
58. Tian, Z.Y.; Vieker, H.; Kouotou, P.M.; Beyer, A. In situ characterization of Cu–Co oxides for catalytic application. *Faraday Discuss.* **2015**, *177*, 249–262. [CrossRef]
59. Li, X.; Xin, M.; Guo, S.; Cai, T.; Du, D.; Xing, W.; Zhao, L.; Guo, W.; Xue, Q.; Yan, Z. Insight of synergistic effect of different active metal ions in layered double hydroxides on their electrochemical behaviors. *Electrochim. Acta* **2017**, *253*, 302–310. [CrossRef]
60. Lenglet, M.; D'huysser, A.; Bonelle, J.P.; Dürr, J.; Jørgensen, C.K. Analysis of X-Ray Ni Kβ Emission, XANES, XPS, Ni 2p, and Optical Spectra of Nickel(II) Spinels and Structure Inference. *Chem. Phys. Lett.* **1987**, *136*, 478–482. [CrossRef]
61. Huang, J.; Qian, W.; Ma, H.; Zhang, H.; Ying, W. Highly selective production of heavy hydrocarbons over cobalt–graphene–silica nanocomposite catalysts. *RSC Adv.* **2017**, *7*, 33441–33449. [CrossRef]
62. Amri, A.; Duan, X.F.; Yin, C.Y.; Jiang, Z.T.; Rahman, M.M.; Pryor, T. Solar absorphance of copper-cobalt oxide thin film coatings with nano-size, grain-like morphology: Optimization and synchrotron radiation XPS studies. *Appl. Surf. Sci.* **2013**, *275*, 127–135. [CrossRef]
63. Li, D.; Gong, Y.; Zhang, Y.; Luo, C.; Li, W.; Fu, Q.; Pan, C. Facile Synthesis of Carbon Nanosphere/$NiCo_2O_4$ Coreshell Sub-microspheres for High Performance Supercapacitor. *Sci. Rep.* **2015**, *5*, 12903. [CrossRef] [PubMed]
64. Suen, N.T.; Hung, S.F.; Quan, Q.; Zhang, N.; Xu, Y.J.; Chen, H.M. Electrocatalysis for the oxygen evolution reaction: Recent development and future perspectives. *Chem. Soc. Rev.* **2017**, *46*, 337–365. [CrossRef]